UNIVERSITY OF AMSTERDAM

UvA-DARE (Digital Academic Repository)

Low-frequency Radio Absorption in Tycho's Supernova Remnant

Arias, M.; Vink, J.; Zhou, P.; de Gasperin, F.; Hardcastle, M.J.; Shimwell, T.W.

DOI
10.3847/1538-3881/ab4f80

Publication date
2019

Document Version
Submitted manuscript

Published in
Astronomical Journal

Link to publication

Citation for published version (APA):
Arias, M., Vink, J., Zhou, P., de Gasperin, F., Hardcastle, M. J., & Shimwell, T. W. (2019). Low-frequency Radio Absorption in Tycho's Supernova Remnant. *Astronomical Journal*, *158*(6), Article 253. https://doi.org/10.3847/1538-3881/ab4f80

General rights
It is not permitted to download or to forward/distribute the text or part of it without the consent of the author(s) and/or copyright holder(s), other than for strictly personal, individual use, unless the work is under an open content license (like Creative Commons).

Disclaimer/Complaints regulations
If you believe that digital publication of certain material infringes any of your rights or (privacy) interests, please let the Library know, stating your reasons. In case of a legitimate complaint, the Library will make the material inaccessible and/or remove it from the website. Please Ask the Library: https://uba.uva.nl/en/contact, or a letter to: Library of the University of Amsterdam, Secretariat, P.O. Box 19185, 1000 GD Amsterdam, The Netherlands. You will be contacted as soon as possible.

UvA-DARE is a service provided by the library of the University of Amsterdam (https://dare.uva.nl)

Download date:08 Oct 2026

Draft version November 11, 2019
Typeset using LaTeX **twocolumn** style in AASTeX63

arXiv:1911.02943v1 [astro-ph.HE] 7 Nov 2019

Low-frequency radio absorption in Tycho's supernova remnant

Maria Arias,[1] Jacco Vink,[1,2,3] Ping Zhou,[1] Francesco de Gasperin,[4] Martin J. Hardcastle,[5] and Tim W. Shimwell[6,7]

[1] *Anton Pannekoek Institute for Astronomy, University of Amsterdam, Science Park 904,1098 XH Amsterdam, The Netherlands*
[2] *SRON, Netherlands Institute for Space Research, Sorbonnelaan 2, 3584 CA Utrecht*
[3] *GRAPPA, University of Amsterdam, Science Park 904, 1098 XH Amsterdam, The Netherlands*
[4] *Hamburger Sternwarte, Universität Hamburg, Gojenbergsweg 112, 21029, Hamburg, Germany*
[5] *Centre for Astrophysics Research, School of Physics, Astronomy and Mathematics, University of Hertfordshire, College Lane, Hatfield AL10 9AB, UK*
[6] *ASTRON, Netherlands Institute for Radio Astronomy, Oude Hoogeveensedijk 4, Dwingeloo, 7991 PD, The Netherlands*
[7] *Leiden Observatory, Leiden University, PO Box 9513, 2300 RA Leiden, The Netherlands*

(Received; Revised; Accepted November 11, 2019)

Submitted to ApJ

ABSTRACT

Tycho's SNR is the remnant of the type Ia supernova explosion SN1572. In this work we present new low-frequency radio observations with the LOFAR Low-Band and High-Band Antennae, centred at 58 MHz and 143 MHz, and with an angular resolution of $41''$ and $6''$ respectively. We compare these maps to VLA maps at 327 MHz and 1420 MHz, and detect the effect of low-frequency absorption in some regions of the remnant due to the presence of free electrons along the line-of-sight. We investigate two origins for the low-frequency free-free absorption that we observe: external absorption from foreground, and internal absorption from Tycho's unshocked ejecta. The external absorption could be due to an ionised thin, diffuse cavity surrounding the SNR (although this cavity would need to be very thin to comply with the neutral fraction required to explain the remnant's optical lines), or it could be due to an over-ionised molecular shell in the vicinity of the remnant. We note that possible ionising sources are the X-ray emission from Tycho, its cosmic rays, or radiation from Tycho's progenitor. For the internal absorption, we are limited by our understanding of the spectral behaviour of the region at unabsorbed radio frequencies. However, the observations are suggestive of free-free absorption from unshocked ejecta inside Tycho's reverse shock.

Keywords: Supernova remnants, interstellar medium, Tycho, LOFAR

1. INTRODUCTION

Supernova remnants (SNRs) are the result of the interaction of a supernova explosion with its ambient medium. The X-ray and radio-bright shell characteristic of young SNRs is composed of shocked ambient medium and stellar ejecta. Internal to the reverse shock there can be some stellar ejecta that have yet to encounter the reverse shock (McKee 1974). These ejecta were initially heated by the passage of the blast wave inside the star, but have since cooled due to adiabatic expansion. Because this material is internal to a shell bright in X-rays and likely also in the UV, it can be photoionised. Several hundreds of years after the supernova event, the remnant still retains some imprint of the explosion; this is particularly the case for the unshocked ejecta.

SNRs have an effect on their surroundings, not only on the shocked ambient medium, but also on the still to-be-shocked neighbourhood of the SNR. They are bright X-ray sources, as well as likely the sites of cosmic ray acceleration (Hillas 2005). Both the high-energy photons and the cosmic rays can deposit energy into the surroundings of the SNR; for instance, heating and ionising nearby molecular clouds. Furthermore, during its lifetime and its pre-SN stage, the progenitor star sculpts

Corresponding author: Maria Arias
M.AriasdeSaavedraBenitez@uva.nl

its ambient medium; for example, through stellar winds and ionising radiation. The environment of the SNR is therefore a diagnostic of the star's pre-SN life, and of the SNR itself.

Tycho's SNR (SN 1572, G120.1+1.4, hereafter Tycho) is a young SNR, whose reverse shock might not have yet heated all of the stellar ejecta from the explosion. It is the result of a Type Ia event, as evidenced from the historical records of the light curve (Baade 1943), and from the optical spectrum as recovered from light echoes (Krause et al. 2008; Rest et al. 2008). From comparison of the X-ray spectra to hydrodynamical and spectral models, Badenes et al. (2006) concluded that the scenario that best fit the data is one in which 1.3 $M_\odot$ of material were ejected at the time of the explosion into an ambient density of $\sim 0.6-3$ cm^{-3}. There is evidence that the density is higher in the north-east of the remnant, from Hα (Ghavamian et al. 2000), molecular gas (Lee et al. 2004; Zhou et al. 2016), and dust observations (Williams et al. 2013). The work of Woods et al. (2017) placed strict upper limits on the temperature and luminosity of Tycho's progenitor from the observed fraction of neutrals in the atomic gas, pointing to the merger of a double white dwarf binary as the most viable scenario for Tycho's SN explosion. On the other hand, the molecular shell found in Zhou et al. (2016) is more consistent with a single-degenerate scenario.

The remnant has been studied extensively, including at wavelengths that probe the unshocked ejecta. Lopez et al. (2015) observed it with *NuStar*, but they did not not detect any emission associated with the decay of radioactive ^{44}Ti, point-like or extended. Gomez et al. (2012) observed it in the infrared with *Herschel* and *Spitzer*, and did not detect a cool dust component in the innermost region of unshocked ejecta, although they did not specifically look for line emission from photoionised, cold material. At low radio frequencies it has been observed with the Very Large Array (VLA) at 330 MHz (Katz-Stone et al. 2000), and several times at 1.4 GHz (Reynoso et al. 1997; Katz-Stone et al. 2000; Williams et al. 2016). It has also been observed at 660 MHz with the Westerbork Synthesis Radio Telescope (WSRT, Duin & Strom 1975), and, at lower resolution, at 408 MHz as part of the Canadian Galactic Plane Survey (CGPS, Kothes et al. 2006).

In this paper we present new observations of Tycho with the LOw Frequency ARray (LOFAR, van Haarlem et al. 2013), both with the instrument's High-Band Antenna (HBA, $120-168$ MHz) and the Low-Band Antenna (LBA, $40-75$ MHz). We compare these maps with higher frequency observations, and we detect localised free-free absorption from free electrons along the line-of-sight, from foreground material, and possibly also from material internal to the SNR reverse shock. We cannot use the measured absorption value to estimate how much mass there is in unshocked ejecta, although our results suggest that if unshocked material is present, it is in a combination of relatively highly ionised, cold, and significantly clumped states. The ionised ambient material could be either the diffuse cavity surrounding Tycho or its neighbouring molecular clouds. Both scenarios have implications for the ionising source.

2. OBSERVATIONS AND DATA REDUCTION

2.1. *Observations*

We observed Tycho's SNR with LOFAR under project LC10_011. The Low-Band Antenna (LBA) observations were centred at RA=00:25:21.5, Dec=+64:08:26.9, with a time on-source of 10 hours. The data were taken on 2018/05/18, in the LBA-Outer configuration, using 8 bit sampling, 1 second integration, and a frequency resolution of 64 channels per sub-band. The central frequency was 53.2 MHz, and the total bandwidth was 43.6 MHz. A second beam was placed on calibrator 3C48 for the length of the observation.

For the High-Band Antenna (HBA) observations we made use of the possibility of co-observing with the LOFAR Two Metre Sky Survey (LoTSS, Shimwell et al. 2017). We identified the LoTSS pointing closest to Tycho, P007+64 (centred at RA=00:30:40.8, Dec=+63:36:57.9), and requested that it be observed during LOFAR cycle 10 as part of LC10_011. The observations were made with the standard LoTSS settings: 8 hours on-source, 48 MHz bandwidth, and an additional 10 minutes at the beginning and end of the observations to observe the calibrators (3C48 and 3C147, in this case).

2.2. *Low-Band Antenna*

The LBA data were reduced with the LOFAR Low-Frequency Pipeline (de Gasperin et al. 2019). The pipeline calibrates the calibrator and transfers the solutions to the target, taking into account the main systematic effects in the LOFAR telescope, such as clock drift, polarisation misalignment, ionospheric delay, Faraday rotation, ionospheric scintillation, beam shape, and bandpass.

Due to noise, we had to flag all the data at frequencies less than 40 MHz, as well as two LOFAR stations, CS013 and CS031. From the calibrator solutions we knew that there were very good ionospheric conditions during the observation, with almost no Faraday rotation (the calibrator was observed for the full duration of the observation, so we knew the ionosphere was good

throughout). This allowed us to perform one round of self-calibration from our first image of the source, rather than from a sky model made at a different frequency.

The pipeline split the data into two frequency chunks, one centred at 48.3 MHz, and another centred at 67.0 MHz, which were imaged separately. We imaged the data with `wsclean` (Offringa et al. 2014), which allows for multi-scale, multi-frequency deconvolution with w-projections, and for applying the LOFAR beam. The visibilities were weighted with a Briggs parameter of zero (Briggs 1995). In order to filter out large scale structure and in order to ensure common resolution among the maps, we used a $u-v$ range of $30-5,000$ λ. The two 'full-bandwidth' LBA images centred at 48.3 MHz and 67.0 MHz are shown in Fig. 1.

In addition to the broadband maps, to search for spectral curvature, we made a series of narrow-band images, each 1.3 MHz wide, centred at 40.1, 42.5, 44.8, 47.1, 49.5, 51.8, 54.2, 56.5, 58.9, 61.2, 63.5, 65.8, 66.9, 68.1, 70.5, 72.8, and 75.1 MHz. These maps were also made with a common $u-v$ range of $30-5,000$ λ.

2.3. *High Band Antenna*

The HBA data were reduced in a direction-independent manner with the Pre-Facet Calibration Pipeline (van Weeren et al. 2016), which obtains diagonal solutions towards the calibrator and then performs clock-TEC separation, which distinguishes between clock offsets and drifts, and signal delays due to the electron column density in the ionosphere, and transfers the calibrator amplitudes and clock corrections to the data.

The calibrated data products were then imaged with the latest version of the ddf-pipeline[1] (Shimwell et al. 2019; Tasse in preparation), which is the method used for reducing data from the LoTSS. The pipeline carries out several iterations of direction-dependent self-calibration, using DDFacet for imaging (Tasse et al. 2018) and KillMS for calibration (Tasse 2014a,b; Smirnov & Tasse 2015). The resulting HBA image is shown in Fig. 2. The pipeline also produced three narrow-band images at 128, 144, and 160 MHz. The LOFAR HBA in-band spectral index is unreliable, but in order to use these narrow-band maps in our analysis we bootstrapped the maps to the expected flux densities of neighbouring sources in the field, from the HBA broadband map.

2.4. *Archival data*

We obtained the FITS files for the 327 MHz Very Large Array (VLA) observation of Tycho carried out in 1991-1993 (Katz-Stone et al. 2000), as well as for the 1.4 GHz VLA observation carried out in 2013-2015 (Williams et al. 2016). Katz-Stone et al. (2000) note that their map is sensitive to scales between $8''$ and $30'$, which corresponds to $114-25,800\lambda$s. The Williams et al. (2016) L-band map, combining the VLA A, B, C, and D configurations, is sensitive to scales between $1.3''$ and $16'$ ($212-15,800\lambda$s).

The integrated flux density of the 1382 MHz map from Williams et al. (2016) is 41.7 Jy, and this is the value that we used for the analysis. However, if we directly measure the integrated flux density of the 327 MHz image, it is 121.8 Jy. This is 115% of the expected value for $S_{1\mathrm{GHz}}=56$ Jy and $\alpha=0.58$ (Green 2017), and 117% for $S_{1\mathrm{GHz}}=52.3$ Jy and $\alpha=0.63$, which are the best-fit values we find from a compilation of literature results (see discussion in section 3.1). We do not measure a level of background in the FITS image that accounts for this difference. Unfortunately, Katz-Stone et al. (2000) do not report the integrated flux density for their 327 MHz observation.

Our analysis relies on the localised deviation from power-law behaviour at low frequencies due to free-free absorption from ionised material along the line-of-sight (we discuss the method in detail in section 3.2). The 327 MHz and 1382 MHz maps provide the fit with the information about the spectral behaviour of the source when no absorption is present. If we take the flux density at 327 MHz to be the 121.8 Jy that we measure directly from the FITS file, we find it disproportionately affects the measured absorption, by setting an artificially high spectral index value for any given pixel[2], which then requires a much larger mass of absorbing material to account for the flux densities at LOFAR frequencies. For this reason, we normalised the flux density of the 327 MHz map to 105.7 Jy, according to the best-fit power law results for the compiled literature values as shown in section 3.1.

When comparing interferometric maps, it is important to take into account the scales probed by the different instruments. When the emission is perfectly deconvolved, it is possible to compare higher resolution maps with lower resolution maps by simply smoothing them to a common resolution. However, the short-baselines $u-v$ coverage matters if interferometers do not probe the same scales, especially for Galactic observations, for

[1] Version 2.2, https://github.com/mhardcastle/ddf-pipeline/

[2] The 121.8 Jy and 41.7 Jy values at 327 MHz and 1382 MHz correspond to a spectral index $\alpha_{327/1382}=0.74$, much higher than the overall spectral index of the source.

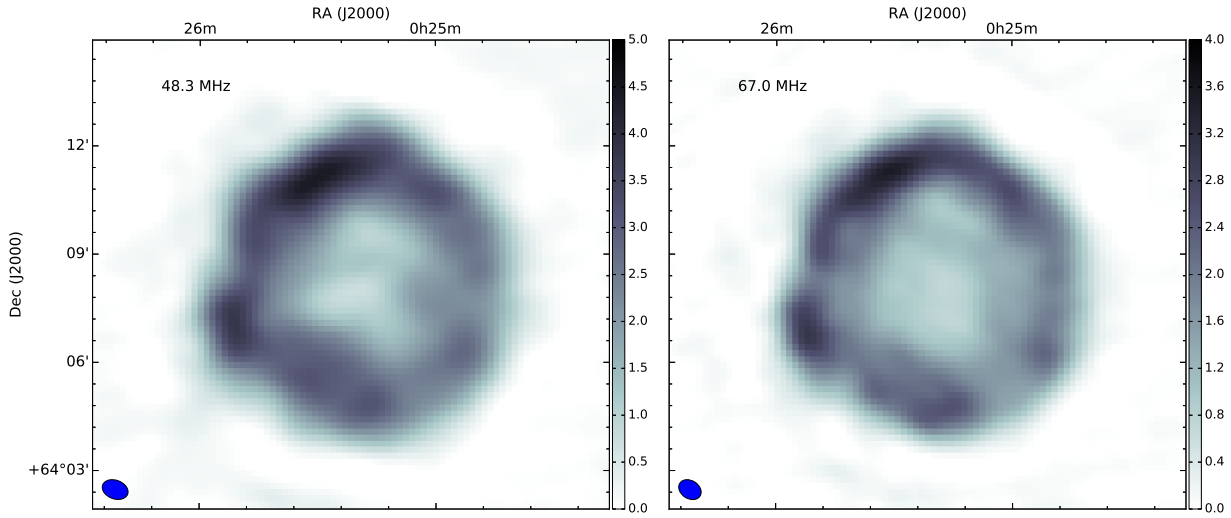

Figure 1. Tycho SNR as observed with the LOFAR Low-Band Antenna (LBA). The LBA bandwidth was split to make these two images, centred at 48.3 MHz (left) and 67.0 MHz (right), each 18 MHz wide. The elliptical beam size is $41'' \times 31''$, with position angle 56°, and the pixel size is $10''$for both maps. The local rms noise is 0.03 Jy bm^{-1} for the 67.0 MHz map and 0.08 Jy bm^{-1} for the 48.3 MHz map. The flux density scale in both maps is in Jy bm^{-1}.

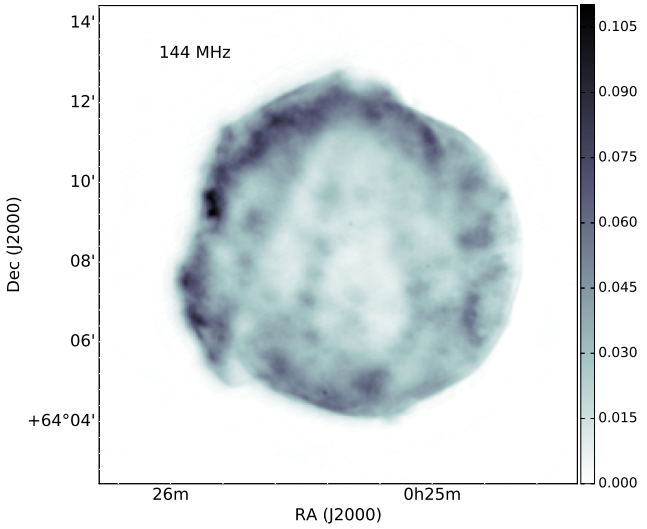

Figure 2. Tycho SNR as observed with the LOFAR High-Band Antenna (HBA). The central frequency is 144 MHz, the bandwidth is 48 MHz, the beam size is $6''$, the pixel size is $1.5''$, and the local rms noise is 1 mJy bm^{-1}. The flux density scale is in Jy bm^{-1}.

which the sources might be embedded in large-scale diffuse emission.

We summarise the $u-v$ scales probed by the maps used in our analysis in Table 1. Our LOFAR maps are sensitive to large angular scales, which might result in additional large-scale continuum emission that is resolved out by the VLA maps. This would result in a spectral index steepening. We note this issue as a possible source of error.

3. RESULTS

3.1. *Total flux density*

We report the total flux density of Tycho as seen with the LOFAR telescope LBA and HBA in Table 1. We also include the values from the 327 MHz and 1382 MHz VLA observations (Katz-Stone et al. 2000; Williams et al. 2016) which we relied on for the analysis.

Table 1. Flux densities of Tycho SNR

Freq (MHz)	Flux density (Jy)	Error (Jy)	Year	λ coverage
48.3	334	33	2018	$30-5,000\ \lambda$
67.0	275	27	2018	$30-5,000\ \lambda$
144.6	163	16	2018	$50-50,000\ \lambda$
327	105.7	10.5	1995	$114-25,800\lambda$
1382	41.7	4.2	2013	$212-15,800\lambda$

NOTE—Observations at 327 MHz and 1382 MHz were taken with the VLA and are described by Katz-Stone et al. (2000) and Williams et al. (2016), respectively. See discussion in section 2.4 for 327 MHz flux density.

We compiled a series of radio flux densities in the literature, and plotted the LOFAR values alongside them (Fig. 3). Fitting a function of the form $S_\nu = S_{1\mathrm{GHz}} \left(\frac{\nu}{1\mathrm{GHz}}\right)^{-\alpha}$ gives a best-fit $S_{1\mathrm{GHz}} = 52.3 \pm 2.0$ Jy

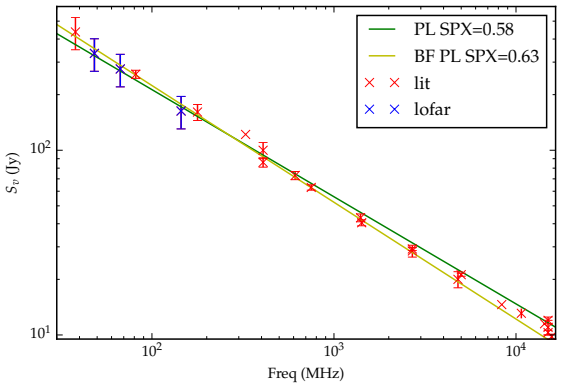

Figure 3. Radio spectrum of Tycho, including measurements from this work (in blue). The green line corresponds to the power-law spectral index (PL SPX) of 0.58 reported in Green (2017), and the yellow line is the best-fit (BF) power-law spectral index from these data points. The literature (lit) values in red are taken from: Klein et al. (1979), Green et al. (1975), Hurley-Walker et al. (2009), Katz-Stone et al. (2000), Kothes et al. (2006), Planck Collaboration et al. (2016), Gao et al. (2011), Langston et al. (2000), Williams et al. (1966), Scott & Shakeshaft (1971), Artyukh et al. (1969), Bennett (1963), Fanti et al. (1974), Conway et al. (1965), Kellermann et al. (1969), Horton et al. (1969).

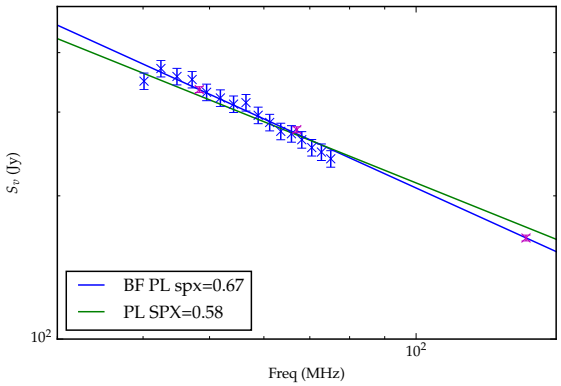

Figure 4. Radio spectrum of Tycho at LOFAR frequencies. The magenta points correspond to the full bandwidth maps, and the blue points correspond to the narrow band maps. The green line corresponds to the power-law spectral index (PL SPX) of 0.58 reported in Green (2017), and the blue line is the best-fit (BF) power-law spectral index from the LOFAR data points. The errors bars have been normalised so the reduced χ^2 of the best-fit power-law (in blue) is equal to 1, but we note that the uncertainties in the LOFAR in-band have not been systematically analysed and can be unreliable. Our measurements agree with earlier reports that the radio spectrum of Tycho steepens at low radio frequencies.

and $\alpha = 0.63 \pm 0.02$, whereas the value listed in the Green SNRs catalogue is $S_{1\mathrm{GHz}} = 56$ Jy and $\alpha = 0.58$ (Green 2017).

The systematic calibration errors in the LOFAR flux scale are of the order of 10%, which dominates the uncertainties, rather than the noise. For this reason we take 10% errors when we report the integrated flux densities of Tycho in the broadband images in Table 1 and in Fig. 3. However, the 10% errors are on the total flux scale rather than the disagreement between in-band measurements. They are therefore an over-estimate for the purposes of our analysis (our fits result in residuals that are much smaller than the error bars). The fact that we do not know the statistical errors of the flux densities presents an issue for the analysis.

In order to solve this problem, we artificially shrank the error bars of the LOFAR images (see Fig. 4) until the reduced χ^2 of the best-fit power-law for these points was 1. This provides us with a more meaningful estimate of the errors in our pixel-by-pixel analysis.

The flux densities of the LBA narrow-band maps are plotted in Fig. 4. If we only consider the LOFAR LBA and HBA results, we measure a steeper spectral index than when we take into account measurements at higher frequencies ($\alpha = 0.67$ instead of $\alpha = 0.58$ or $\alpha = 0.63$). The best-fit value of α for the LOFAR points ($\alpha = 0.63$) results in a $\Delta\chi^2 = 23.7$ improvement over the fixed $\alpha = 0.58$ scenario, for one additional degree of freedom.

3.2. *Model parameters: external absorption*

A synchrotron source with spectrum $S_\nu \propto \nu^{-\alpha}$ that is subject to free-free absorption from cold, ionised, ISM material along the line of sight results in the following radio spectrum:

$$S_\nu = S_0 \left(\frac{\nu}{\nu_0}\right)^{-\alpha} e^{-\tau_{\nu,\mathrm{ISM}}}, \quad (1)$$

where (Rybicki & Lightman 1979):

$$\tau_\nu = 3.014\times10^4\, Z \left(\frac{T}{\mathrm{K}}\right)^{-3/2} \left(\frac{\nu}{\mathrm{MHz}}\right)^{-2} \left(\frac{EM}{\mathrm{pc\,cm^{-6}}}\right) g_{\mathrm{ff}}, \quad (2)$$

Ze is the charge of the free-free absorbing ions, T is the temperature of the plasma, $EM \equiv \int_0^s n_\mathrm{e}^2 ds'$ is the emission measure, n_e is the number density of electrons, and g_{ff} is a Gaunt factor, given by

$$g_{\mathrm{ff}} = \begin{cases} \ln\left[49.55\, Z^{-1} \left(\frac{\nu}{\mathrm{MHz}}\right)^{-1}\right] + 1.5 \ln \frac{T}{\mathrm{K}} \\ \\ 1 \qquad\qquad \text{for } \frac{\nu}{\mathrm{MHz}} >> \left(\frac{T}{\mathrm{K}}\right)^{3/2}. \end{cases} \quad (3)$$

We convolved all the images to a resolution of 41″, and performed a pixel-by-pixel fit (with a pixel size of 10″)

to equation 1. The results are plotted in Fig. 5. For each pixel, we fitted for an amplitude S_0, the spectral index α, and the optical depth for the ISM material at 40 MHz $\tau_{40,\rm ISM}$. As errors, we plot the diagonal term of the covariance matrix corresponding to each parameter.

We also show the fit results for three integrated regions that show external absorption (see Fig. 5, right panel): the region towards the north-east, the absorbed region in the centre, and the whole rim of the SNR. These regions are labeled in Fig. 6, and their spectral energy distribution (SED) along with the best-fit results are shown. The parameters α and $\tau_{40,\rm ext}$ are correlated (see contour plots in Fig. 7), but for two of the three regions we require absorption at the 3σ level or higher.

3.3. *Model parameters: internal absorption*

A synchrotron source that is subject to internal free-free absorption from its cold, ionised, unshocked ejecta will have a dimming factor that goes as $(f+(1-f)e^{-\tau_\nu})$, where f is the fraction of the synchrotron emission that is produced by the front side of the shell and, therefore, cannot be absorbed by its internal material. This factor multiplies equation 1 resulting in the following radio spectrum:

$$S_\nu = S_0 \left(\frac{\nu}{\nu_0}\right)^{-\alpha} (f + (1-f)e^{-\tau_{\nu,\rm int}})\, e^{-\tau_{\nu,\rm ISM}}. \quad (4)$$

Internal free-free absorption can only occur in the region inside the projected reverse shock, since there cannot be unshocked absorbing material outside the reverse shock. Warren et al. (2005) found the reverse shock in Tycho's SNR to have a radius of 183″ and centre RA=0:25:19.40, Dec=+64:08:13.98, from principal component analysis of X-ray data. We measured the flux density for each image for the region internal to the reverse shock, with the aim to look for internal absorption. We do not find any external absorption in the region internal to the reverse shock, save for two clumps in the center of the SNR (Fig. 5), and so, to simplify our fit, we we removed the area of absorption in the centre (the blue region in Fig. 6) from our area of internal absorption (the yellow region in Fig. 6), and just fitted for an amplitude, the parameter f, and an internal optical depth:

$$S_\nu = S_0 \left(\frac{\nu}{\nu_0}\right)^{-\alpha} (f + (1-f)e^{-\tau_{\nu,\rm int}}). \quad (5)$$

As described in section 3.1, we rescaled the error bars in such a way that the reduced χ^2 of the best-fit power-law ($S_\nu = S_0 \left(\frac{\nu}{\nu_0}\right)^{-\alpha}$, with no absorbing component) was 1. The best-fit power-law for this region corresponds to $\alpha = 0.63$. From here, we compared how including an internal absorbing component improved the fit.

Setting $f = 0.5$ (that is, fixing the synchrotron emission such that half comes from the back and half comes from the front of the shell) gives a best-fit $\alpha = 0.63$, $\tau_{40,\rm int} = 3\times10^{-8}$. This means that the best-fit value for internal absorption with $f = 0.5$ corresponds to no internal absorption. Setting $f = 0.5$, for $\tau_{40,\rm int} = 0.11$ we obtained a $\Delta\chi^2 = 4$ (with respect to the best-fit result). We take this to be the 2σ upper limit estimate on the internal optical depth, and so in the internal emission measure $EM_{\rm int}$ (for $T = 100$, $Z = 3$).

Alternatively, if we fit a region that shows internal absorption with a power-law, the spectral index flattens due to the presence of absorption. Katz-Stone et al. (2000) found $\alpha = 0.71$, rather than $\alpha = 0.63$ for this region, from a 330 MHz to 1.4 GHz spectral index study. In fact, the higher frequency data points, where no absorption is present, should be the ones that determine the spectral index. At low frequencies the original spectral index should be recovered, but with the amplitude dimmed by a factor of f. Hence, we fixed the spectral index to $\alpha = 0.71$ and fitted for the remaining parameters. This results in a very high value of the optical depth, $\tau_{40,\rm int} = 61$.

Table 2. Fits to region internal to the reverse shock

Fit	α	f	$\tau_{40,\rm int}$	red χ^2	$\Delta\chi^2$
PL	0.63	–	–	1.0	-
best-fit int abs	0.63	0.5*	3×10^{-8}	1.1	0
UL in int abs	0.64	0.5*	0.11	1.3	4
Fixed α	0.71*	0.76	61.1	0.4	16

NOTE—The best-fit emission measure EM assumes T = 100 K and $Z = 3$. Parameterised, it corresponds to $EM = EM_{\rm table}\,{\rm pc\,cm^{-6}} \left(\frac{g_{\rm ff}(T=100,Z=3)}{g_{\rm ff}(T/100\,{\rm K},Z/3)}\right) \times \left(\frac{Z}{3}\right) \left(\frac{T}{100\,{\rm K}}\right)^{-3/2}$. The reduced χ^2 to the power-law fit is 1 by definition. Values indicated with * are fixed, not fitted for. The $\Delta\chi^2$ for the 'Fixed α' model is with respect to the power-law model 'PL', corresponding to 2 additional degrees of freedom. The upper limit 'UL' was derived as discussed in the text.

The results of our fits (power-law, internal absorption, 2σ upper limit in internal absorption, and α fixed to the value given by Katz-Stone et al. 2000) are tabulated in Table 2. We also plotted the results for the power-law fit (in blue), the upper limit to the EM (for $T = 100$, $Z = 3$, in green) and the fixed α (in magenta; dashed

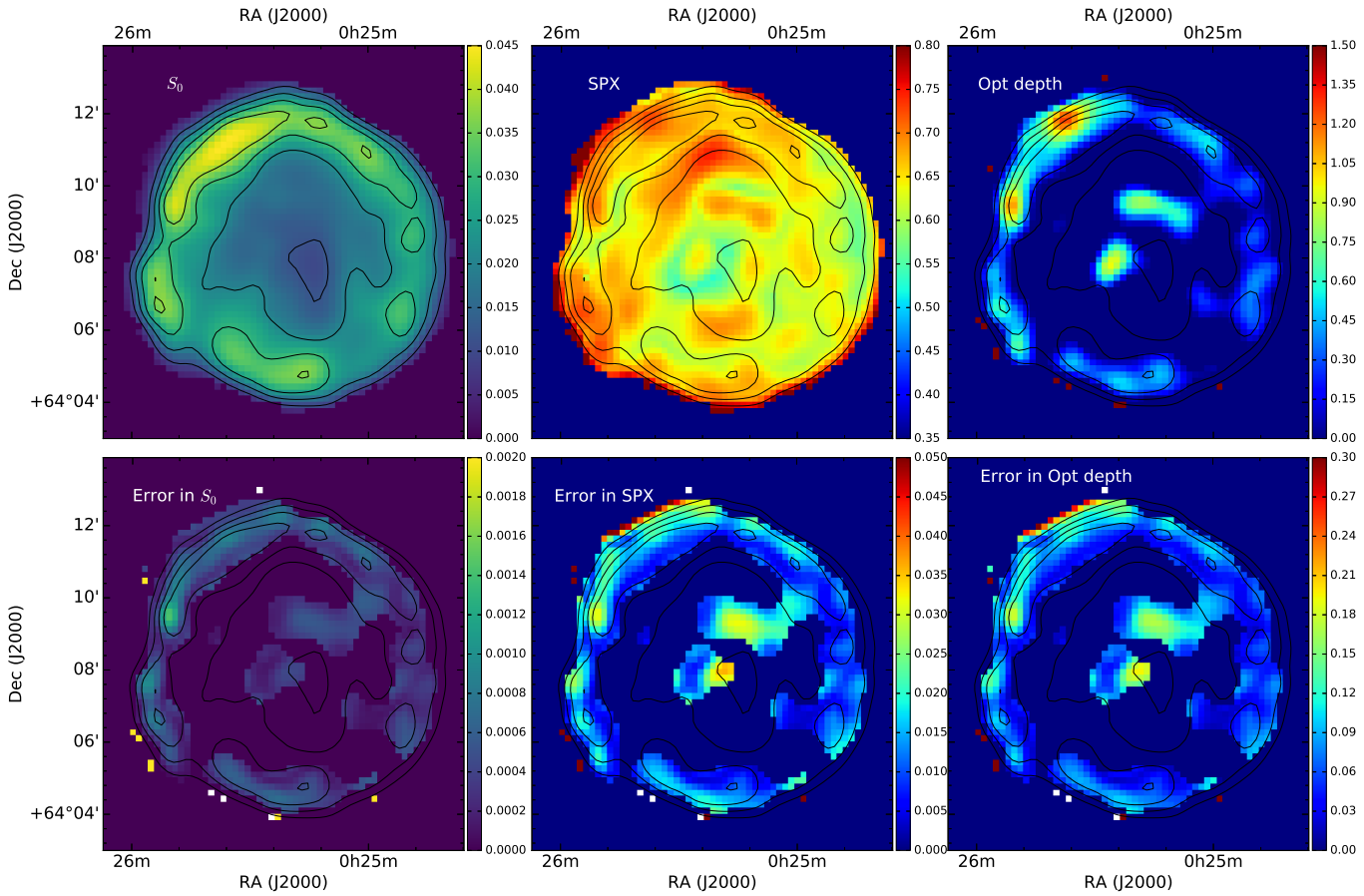

Figure 5. Results of fitting equation 1 to the maps. For each pixel we fitted for amplitude S_0, the spectral index α, and the optical depth for the ISM material at 40 MHz $\tau_{40,\mathrm{ISM}}$. The units of the S_0 map on the left are Jy bm^{-1}. The errors are the diagonal term of the covariance matrix corresponding to each parameter.

lines indicate the unabsorbed flux density) in Fig. 6, bottom-left corner. Here we show the rescaled errors rather than the original error bars.

From Table 2, fixing $\alpha = 0.71$ and adding an absorbing component does seem to significantly improve the fit (the fact that the reduced χ^2 is equal to 0.4 would normally suggest overfitting, but in this case the reduced χ^2 of the power-law fit was artificially set to 1). The required emission measure is unphysical (see discussion in section 4.4), but it is very sensitive to the choice of α and f. We cannot confidently claim a detection of unshocked ejecta in Tycho's SNR because of our limited knowledge of the errors in the flux densities, and because of the degeneracy of the parameters, but our data are suggestive that there is indeed some unshocked material inside Tycho's reverse shock[3].

In order to better estimate the EM due to internal absorption we need more high-frequency data points in the few GHz range that can unambiguously determine the unabsorbed flux density and spectral index for this region. Additional observations in the few-hundred MHz range would help better model the curvature due to the free-free absorption, and, if it were ever possible, observations at even lower frequencies would further discriminate between the different models. In this work we are relying on only the points at 327 MHz and 1382 MHz for information about the unabsorbed flux density and

[3] In the conference Supernova Remnants: An Odyssey in Space after Stellar Death II (Chania, Greece, June 2019) we presented preliminary results of a very high EM detection from Tycho's unshocked ejecta (http://snr2019.astro.noa.gr/wp-content/uploads/2019/08/D3-0940-Arias.pdf). This was due to us not noticing at first that the 330 MHz map had a very high flux density value, which steepened the best-fit spectral index, and thus the required amount of absorbing material.

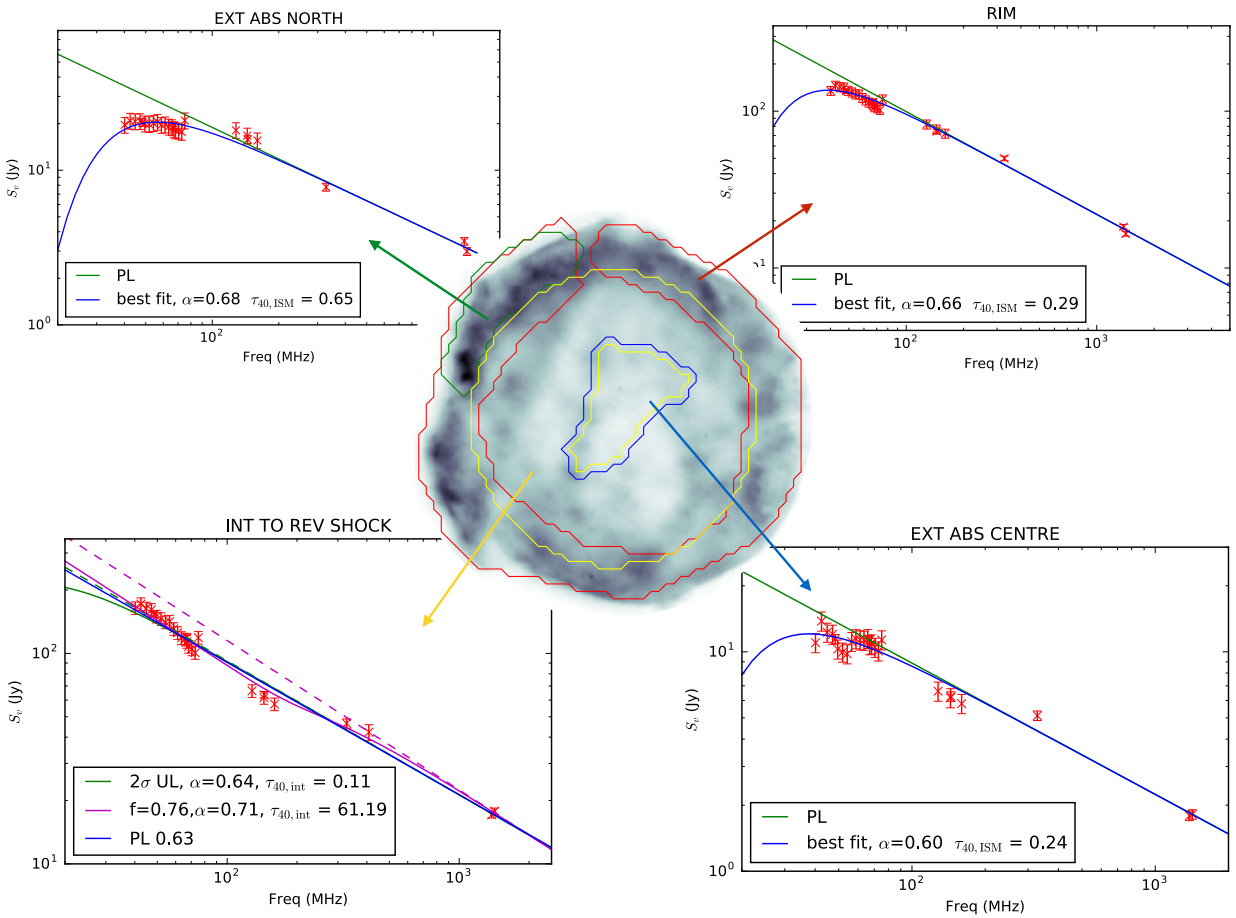

Figure 6. HBA map with overlaid regions of analysis. The values of f, τ_{40} and α are unitless. For all regions, the errors were rescaled in such a way that the best-fit power law has a reduced χ^2 of 1. The top plots and the bottom-right plot (corresponding to the green, red, and blue regions as overlaid on Tycho) are fitted including external absorption (in blue, the best-fit unabsorbed power-law is in green), and in all cases including the absorption term improves the fit: with a $\Delta\chi^2 = 16$ for 'EXT ABS NORTH', a $\Delta\chi^2 = 4$ for 'EXT ABS CENTRE', and a $\Delta\chi^2 = 10.5$ for 'RIM' (in all cases, for an additional degree of freedom). The bottom-left plot corresponds to the region of possible internal absorption. The mask of the reverse shock radius is plotted in yellow over the map of Tycho. In the legends, 'UL' stands for 'upper limit' and 'PL' stands for 'power-law'.

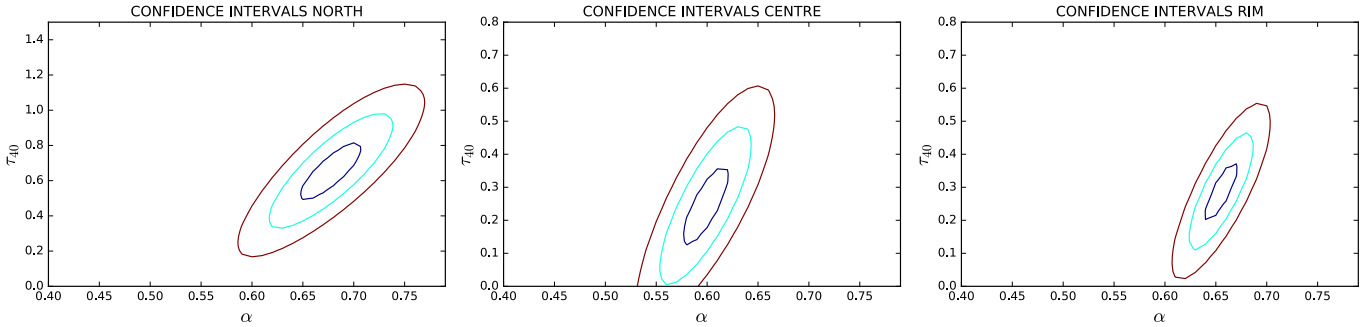

Figure 7. Contour plots for the three regions showing external absorption in Fig. 6: north (shown in red over Tycho in Fig. 6), centre (in blue), and rim (in red). Plotted are the 1σ, 2σ, and 3σ confidence intervals for the parameters α and $\tau_{40,\mathrm{ext}}$ for each of the regions. Only for one region, centre, $\tau_{40,\mathrm{ext}} = 0$ (no absorption) is not excluded at the 3σ. For the two other regions, in particular for the northern region that we base our analysis on, we require the presence of absorption along the line-of-sight at the 3σ level.

spectrum, and the 327 MHz map was rescaled (see discussion in section 2.4). Moreover, the behaviour of the LOFAR in-band seems to be pushing the data point in a steeper spectral index direction. For this reason, observations that increase the leverage arm in frequency would allow us to better constrain the amount of EM due to unshocked material.

Having said that, the integrated flux densities as measured by LOFAR are in line with what we expect from the literature. There are some regions where the maps can have artefacts, but the flux densities that we are considering in this section are taken from the yellow region in Fig. 6, which is much larger than the resolution of any given map. Moreover, the LBA and the HBA data both show the effect of absorption, even though the two LOFAR antennas are effectively different instruments, and the data were reduced with two independent pipelines.

4. DISCUSSION

4.1. *Spectral index*

Katz-Stone et al. (2000) carried out a study of Tycho's spectral index at low radio frequencies (330 MHz and 1.5 GHz), and found that Tycho has localised spectral variations with regions as flat as $\alpha = 0.44$ and as steep as $\alpha = 0.72$. Our best-fit spectral index map (middle panel in Fig. 5) shows values within this range, and, in a few cases, slightly higher values, $\alpha \lesssim 0.8$.

Duin & Strom (1975) reported a significant steepening of the spectrum near the centre of the SNR and suggested that particles near the boundary might be accelerated with a flatter spectrum, but Klein et al. (1979) did not find steepening in their observations at 10 GHz. We do not find a steepening coincident with the centre of the remnant, but rather we find the spectrum of the western and north-western region of the remnant to be steeper than the rest.

The question of whether Tycho has a curved spectrum has been discussed in the literature. Roger et al. (1973) modelled Tycho's integrated radio spectrum with two power-law components (which results in a locally concave spectrum), Reynolds & Ellison (1992) modelled it with a non-linear shock model of first-order Fermi acceleration and found agreement with a concave-up synchrotron spectrum, whereas Vinyaikin et al. (1987) found that a single power-law can describe the radio spectrum at these frequencies. As we discussed in section 3.1, the LOFAR data points do show a steeper spectral behaviour than expected, although the in-band response of the LOFAR LBA has not been systematically analysed, and is not yet reliable.

4.2. *External absorption*

In order to convert the value of optical depth in Fig. 5 into a quantity that allows us to derive physical properties of the gas we use equation 2, from which we obtain an emission measure value, $EM_{\rm ISM}$. The emission measure depends on the temperature and ionisation state of the plasma. The ISM has a wide range of temperatures, from ~ 10 K in molecular clouds to $\sim 10,000$ K in the warm ionised medium (Draine 2011). We therefore provide three emission measure maps in Fig. 8, assuming $T = 10$ K, $T = 100$ K, and $T = 10,000$ K, to aid our discussion in the current section. Since the ISM is primarily composed of hydrogen, for all three maps we assume $Z = 1$.

The region to the north-east with the high emission measure value (the region in green in Fig. 6) seems to match the position of a molecular cloud found in Lee et al. (2004) and Zhou et al. (2016), seen most clearly in Fig. 1 of the latter paper at velocities between -62 km s^{-1} and -66 km s^{-1}. At these velocities there are also multiple structures that coincide in position with the rim of the source, which our fit also identifies as having free-free absorption. The region in the north-east of the remnant where we find the highest values of the $EM_{\rm ISM}$ also coincides with the region of high H I absorption seen in Reynoso et al. (1999). The region in the centre of Tycho has some morphological coincidence with the molecular structure seen at -56 km s^{-1} in Zhou et al. (2016), although the similarity is not striking, and there does not seem to be any associated neutral hydrogen structure. Our method traces ionised material, which one does not expect in molecular clouds but could be present at their outer boundary, so it is not necessary that our measured $EM_{\rm ISM}$ matches the structure of molecular/neutral material in detail.

The scale and distance of the ionised features are not straightforward from these observations. Tycho is the background synchrotron source, so the ionised material must be in front of it, but in principle it could be local to Tycho, unrelated ISM, or a combination of the two (although it would be a big coincidence if one of the two did not have a dominant effect).

We know from Zhou et al. (2016) that Tycho is likely inside an expanding wind bubble that is sweeping up molecular material. We depict the structure we assume for our analysis in a cartoon in Fig. 9. The remnant is surrounded by, but its shock is still not interacting with, molecular clouds. This means that there is a cavity of thickness l (and radius $R_{\rm SNR}+l$) of low-density material ($\rho = 0.1 - 0.2$ cm^{-3}, Williams et al. 2013), surrounded by dense molecular material with an average density of $10^2 - 10^3$ cm^{-3} (Zhou et al. 2016).

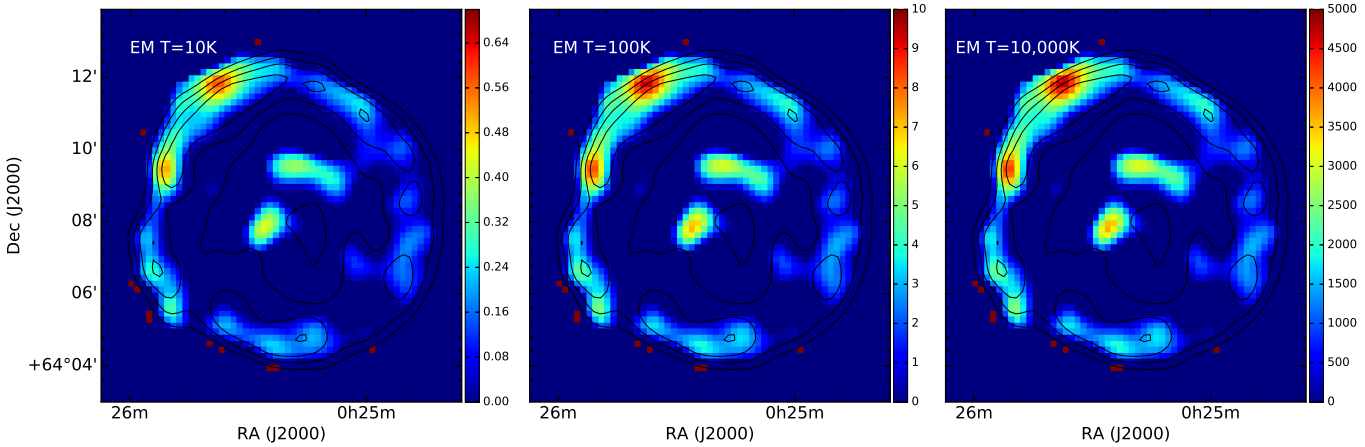

Figure 8. Maps of external emission measure $EM_{\rm ISM}$ made from the measured optical depth $\tau_{40,\rm ISM}$ (right hand side map in in Fig. 5) combined with equation 2, assuming $Z = 1$. We plot the results for three temperatures, 10 K, 100 K, and 10,000 K, relevant for our discussions of molecular clouds, the diffuse, infrared-emitting medium around Tycho, and the ISM warm ionised gas, respectively. The units of $EM_{\rm ISM}$ are $\rm pc\,cm^{-6}$.

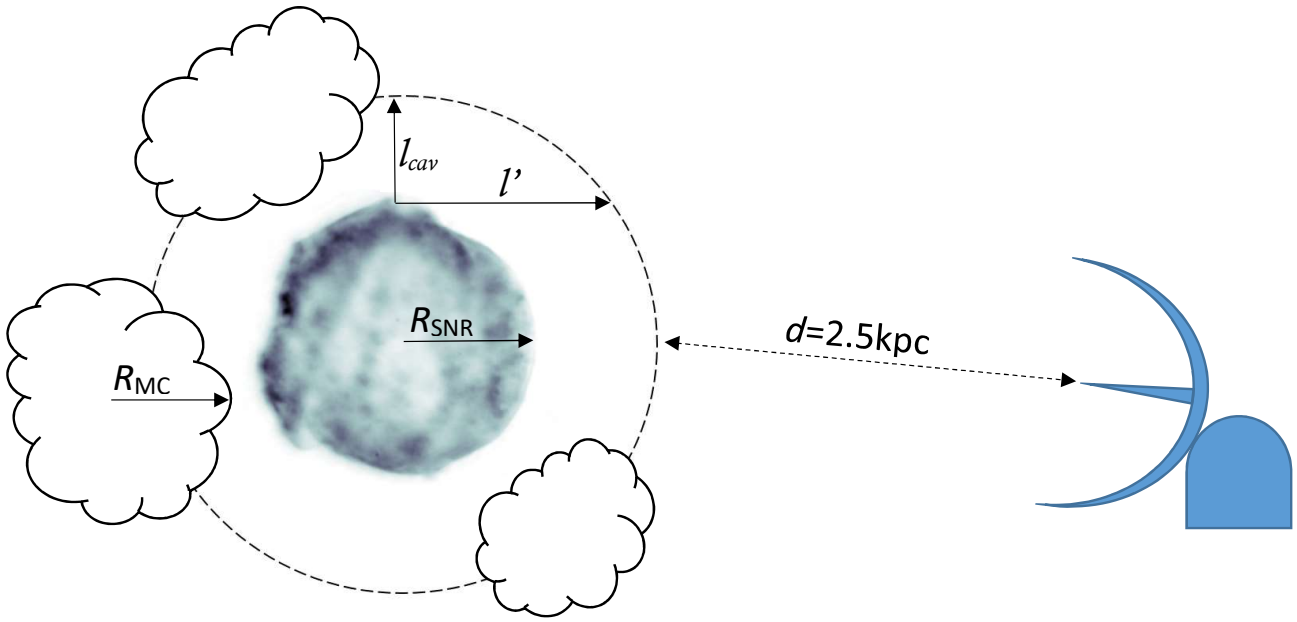

Figure 9. Cartoon showing the geometry assumed for the discussion in section 4.2. Tycho is surrounded by a diffuse cavity of length $l_{\rm cav}$, and the molecular clouds are in a ring-like shape around it.

We will consider three possibilities: (1) that the ionised material we see in Fig. 5, right-hand side, is due to ionised material along the line-of-sight, unrelated to Tycho; (2) that it is the low-density cavity material that is ionised; and (3) that the molecular clouds are responsible for the free-free absorption. In section 4.3 we briefly mention possible ionising sources.

1. Ionised ISM

Hwang et al. (2002) tabulated the $N_{\rm H}$ as measured from *Chandra* data, towards Tycho, and found values ranging from $N_{\rm H} = (5.3 - 7.5) \times 10^{21}$ cm^{-2}, depending on the model employed.

For the region in green in Fig. 6 the optical depth at 40 MHz is $\tau_{40,\rm ISM} = 0.65$, which corresponds to an emission measure of $EM = 0.30$ pc cm^{-6} for $T = 10$ K, and $EM = 2469$ pc cm^{-6} for $T = 10,000$ K. Since $EM = n_{\rm e}^2 l$, $N_{\rm H} = n_{\rm H} l$, and $n_{\rm e} = \chi_{\rm e} n_{\rm H}$ (where $\chi_{\rm e}$ is the ionisation fraction, $0 \leq \chi_{\rm e} \leq 1$), then, using $l = d$, the distance to Tycho, we find that the required ionisation fraction of the intervening ISM is

$\chi_e = \frac{\sqrt{EM\,l}}{N_H} \sim 0.015\sqrt{\frac{l}{2.5\,\mathrm{kpc}}}$ for $T = 10$ K, or alternatively, $\chi_e \sim 1.35\sqrt{\frac{l}{2.5\,\mathrm{kpc}}}$ for $T = 10{,}000$ K. The 10,000 K assumption for the diffuse ISM gas is more reasonable than the 10 K (Draine 2011), although, of course, this gas does not extend evenly along the line-of-sight to Tycho, but is likely in a patchy distribution (which would lower χ_e to a more reasonable value). We do not know the relative depths of these warm ionised gas along the line-of-sight to Tycho, so unfortunately we cannot constrain a χ_e for the case of this ISM.

Another point to note is that $\tau_{40,\mathrm{ISM}} = 0.65$ corresponds to an optical depth of $\tau_{30.9} = 1.2$ at 30.9 MHz, although this is for a very small area (3.6 arcmin^2). Kassim (1989) studied optical depths towards 15 Galactic SNRs, and found only once source with $\tau_{30.9} > 1$. The integrated radio spectrum of Tycho (Fig. 3) shows no indication of free-free absorption from the ISM kicking in at frequencies lower than 100 MHz. There is a slight drop visible in the spectrum from LOFAR narrow band maps (Fig. 4), although this relies only on the data point at 40 MHz. For the integrated spectrum of Tycho's SNR we measure a best-fit $\tau_{30.9} = 0.1$, well on the low side of the values measured by Kassim (1989).

The relatively high value of the optical depth in the region in green in Fig. 6, and its small area suggest that this is a small clump of ionised material. We cannot know if the clump is relatively close to the source or somewhere along the line-of-sight.

Finally, the low-frequency absorption is only seen in a ring-like structure in the rim of the SNR and in two clumpy regions in the SNR centre. In the remaining regions in the interior we do not find any detectable absorption. It is unlikely, though, that the foreground ISM gas has the shape we see over Tycho, with a clear ring and a mostly empty interior. The regular morphology seen in the maps in Fig. 8 does not favour the ionised ISM scenario as the dominant source of absorption.

2. Ionised diffuse cavity surrounding Tycho

Consider that it is the cavity surrounding Tycho that is responsible for the ionisation we see at LOFAR frequencies.

The size of the ionised cavity may influence the distributions of the foreground absorption. As shown in figure 9, the depth of the ionised materials l' is as a function of the projection radius r ($r = 0$ at the SNR center, $r = R$ at the SNR boundary), the radius of the SNR R and the thickness of the cavity l ($l' = \sqrt{l^2 + 2lR}$), resulting in:

$$l'(R) \approx \begin{cases} \sqrt{2Rl}, & \text{if } l \ll R \\ l, & \text{if } l \gg R \end{cases} \tag{6}$$

$$l'(0) = l. \tag{7}$$

If the cavity size is much larger than the SNR radius, we would see a uniform ionisation distribution as $l'(r) = l$. The ring-like ionisation distribution suggests that the cavity is small and might be close to the SNR radius.

Williams et al. (2013) found that the ISM density around Tycho is only $n_H = 0.1 - 0.2$ cm^{-3}, and that there is dust with temperature $T = 100$ K.

The optical depth value we report for the rim of Tycho (the region in red in Fig. 6), $\tau_{40,\mathrm{ISM}} = 0.29$, assuming $Z = 1$ and $T = 100$ K, corresponds to an emission measure of $EM = 2.1$ pc cm$^{-6} = n_e^2\, l_{\mathrm{cav}}$, where l_{cav} is the size of the cavity. This implies $n_e = 1.5\sqrt{\frac{l_{\mathrm{cav}}}{1\ \mathrm{pc}}}$ cm^{-3}. Recall that $n_e = \chi_e n_H$.

Woods et al. (2017) measured the ionisation fraction of the ambient hydrogen ahead of the forward shock to be $\chi_e < 0.2$ (the ambient hydrogen is more than 80% neutral). They obtained the ionisation fraction for the atomic gas, which has a higher density; they used $n_H = 1$ cm^{-3}. Setting $\chi_e = 0.2 = \frac{n_e}{n_H}$ means that the cavity must be very small, $l_{\mathrm{cav}} < 0.02$ pc.

As mentioned above, a thin length for l_{cav} is supported by the geometry of the external absorption map, which appears to be limb-brightened. However, this is a very restrictive value, requiring that Tycho be almost but not quite interacting with the molecular cloud, and not just in one place but around its entire perimeter. This is very unlikely.

3. Ionised dense molecular environment surrounding Tycho

In this section we consider whether the ionised structure is related to the molecular cloud found by Lee et al. (2004) and discussed in Zhou et al. (2016). The morphological coincidence of the molecular cloud in the north-east with the region of highest absorption is suggestive of such a relation.

Zhou et al. (2016) tabulate the molecular hydrogen column density N_{H_2} for several positions and find values around 7×10^{20} cm^{-2} in the area where we measure $\tau_{40,\mathrm{ISM}} = 0.65$, implying $EM = 0.30$ pc cm^{-6} (here the conditions $Z = 1$, $T = 10$ K do apply). Since $EM = n_e^2 l$, $N_{H_2} = n_{H_2} l$, and $\chi_e = \frac{n_e}{n_{H_2}}$, the value $\frac{EM}{N_{H_2}} = \chi_e n_e = 4.3 \times 10^{-4}$ cm^{-3} is independent of the size of the molecular cloud.

If we take the size of the molecular clouds to be of the order of Tycho ($l_{\mathrm{MC}} \sim 5$ pc , see Fig. 1, bottom-right in Zhou et al. 2016), then $n_e = 0.25\sqrt{\frac{l_{\mathrm{MC}}}{5\ \mathrm{pc}}}$ cm^{-3}, which corresponds to $\chi_e = 2 \times 10^{-3} \left(\frac{l_{\mathrm{MC}}}{5\ \mathrm{pc}}\right)^{-1/2}$.

Generally, dense molecular cores have $\chi_e \sim 10^{-8} - 10^{-6}$ (Caselli et al. 1998), while translucent and diffuse molecular gas has typical $\chi_e \lesssim 10^{-4}$ (Snow & McCall 2006, figure 1). $\chi_e \sim 10^{-3}$ requires an external ionising source.

It is not possible to tell directly from our observations of free-free absorption whether the ionised absorbing component is in the environs of Tycho or far in the ISM along the line-of-sight. However, the fact that the absorption occurs where the remnant is brighter and expanding into a higher density region (Reynoso et al. 1999; Williams et al. 2013) is suggestive to us of a local effect, as is the rimmed geometry. If the thin cavity surrounding Tycho and separating the SNR shock from the molecular ring were responsible for the absorption, then the cavity would have to be very thin but at the same time the shock could not have reached the molecular material *anywhere* along its boundary —a contrived geometry. The high neutrals values inferred by Woods et al. (2017), the clear presence of Balmer shocks (Ghavamian et al. 2000), and the morphological coincidence with the molecular cloud in the north-east all point towards the molecular material being associated with the absorption. Finally, the bubble-like distribution of the molecular gas provides a natural explanation for the rimmed absorption morphology. We conclude that the absorption is most likely due to the presence of over-ionised molecular clouds.

4.3. *What mechanism is responsible for the ionisation of Tycho's surroundings?*

A SIMBAD query towards the direction of Tycho gives no OB associations or bright stars that could be responsible for the observed ionisation: Tycho itself is the only likely ionising source towards this line-of-sight. The sources of ionisation could be the X-ray emission from Tycho, the cosmic rays accelerated in the SNR, or perhaps the ionising radiation emitted by the supernova progenitor or the event itself. A full discussion of the different ionisation scenarios requires a detailed treatment of ionisation and recombination in the modelling, and is beyond the scope of this paper.

4.4. *Internal absorption and mass in the unshocked ejecta*

The amount of mass in ionised material internal to the SNR reverse shock is given by (see Arias et al. 2018):

$$M = ASl^{1/2} m_p \frac{1}{Z} \sqrt{EM}, \tag{8}$$

where A is the mass number of the ions, S is the area of the region for which we measure the absorption, l is the depth of the absorbing material, m_p is the mass of the proton, Z is the number of charges, and EM is the emission measure. Making certain assumptions about these values, one can derive a value for the mass in unshocked material from our measured optical depth.

The easiest parameter to estimate is the mass number of the ions A. Tycho is the result of a Type Ia explosion; out of the $\sim 1.4\ M_\odot$ of ejecta it produced, $0.5-0.8\ M_\odot$ is expected to be iron (Badenes et al. 2006). In a spectroscopic analysis of ASCA data Hwang et al. (1998) noted that iron is in fact the most recently ionised element, and so it is likely to compose the bulk of the unshocked material. Hayato et al. (2010) also found segregation of Fe in the inner ejecta from a study of the expansion velocities of the X-ray emitting material. Moreover, the X-ray emission from iron in Tycho is not as prominent as in other type Ia SNRs (e.g. Kepler, Reynolds et al. 2007), suggesting that some of it is not visible in the X-rays yet. For these reasons we take $A = 56$, corresponding to Fe. We take $Z = 3$, for three-times ionised Fe.

S is the surface area of the absorbing region (the area in yellow in Fig. 6). We do not know the thickness of the absorbing slab l, which is actually critical for the mass determination, because we do not have a way of probing the three-dimensional structure of the absorbing material. For a homogeneous distribution of material within the sphere of the reverse shock, the average depth is $l = \frac{4}{3}R$ (where R, the radius of the reverse shock, is 2.25 pc for a distance of 2.5 kpc, Tian & Leahy 2011).

Finally, the value of the EM depends on Z and the temperature T. We do not know what the temperature conditions in the unshocked ejecta of Tycho are; an accurate determination would require infrared observations that could measure the ratios between different forbidden lines of the ionised material. To our knowledge, the only time the temperature from the unshocked ejecta of a SNR has been measured is in the case of Cas A, whose unshocked ejecta has a temperature of 100 K (Raymond et al. 2018). Although it is not clear that the radiation from Tycho's SNR could maintain its internal material heated to 100 K, we will take this to be the value in our mass estimate.

The EM values in Table 2 correspond to the following mass estimates:

$$M = 6.5 \pm 2.1\ M_\odot \left(\frac{A}{56}\right) \left(\frac{l}{3.0\,\mathrm{pc}}\right)^{1/2} \left(\frac{Z}{3}\right)^{-3/2} \left(\frac{T}{100\ \mathrm{K}}\right)^{3/4} \times \sqrt{\frac{g_{\mathrm{ff}}(T = 100\,\mathrm{K}, Z = 3)}{g_{\mathrm{ff}}(T, Z)}}, \tag{9}$$

in the case of the upper limit with $EM = 0.33$ pc cm^{-6}, and in the case of $EM = 179$ pc cm^{-6}, $M = 146 \pm 39\ M_\odot$, with the same parametrisation.

4.5. *What are the conditions and structure of the ejecta internal to Tycho's reverse shock?*

Our upper limit above is not useful, and the mass estimate for the $\alpha = 0.71$ fit is completely unreasonable, since the total amount of ejecta resulting from the explosion of Tycho's progenitor was $\sim 1.4\ M_\odot$. As we mention above, a determination of the EM depends very much on the expected flux if no absorption were present, but if there is indeed absorption noticeable at LOFAR HBA frequencies (~ 150 MHz), then the high mass estimate value implies that the conditions we assumed in the section above do not describe the actual physical conditions internal to the SNR reverse shock.

Lowering the temperature or invoking a higher ionisation state alone are not sufficient to arrive at a meaningful mass estimate. A further way to reduce the mass estimate for a given $EM_{\rm int}$ is if not all unshocked material is iron, but lighter elements are also present. Decourchelle (2017) notes that the comparison of iron-L complex and Si-K line images indicates good mixing of the Si and Fe layers synthesised in the supernova. The mass number of Si is half of that of Fe, so if silicon is present, the mass estimate could be significantly reduced.

The effects of temperature, ionisation conditions, and composition can be important if combined, but the single effect that can have the largest contribution to the high absorption value is the degree of clumping in the unshocked material. The estimate in equation 9 assumes that the ejecta are distributed homogeneously within the sphere of the reverse shock. This is what one expects for an ejecta density profile with a flat core and an exponential outer region (Chevalier 1982), if the reverse shock has already reached the core.

Sato et al. (2019) analysed *Chandra* observations of Tycho and found from its genus statistic that Tycho's X-ray ejecta structure strongly indicates a skewed non-Gaussian distribution of the ejecta clumps, possibly from initially clumped ejecta. The radioactive decay of elements synthesised in the explosion could also cause the ejecta to have a foamy distribution, as is the case for Cas A (Milisavljevic & Fesen 2015). If the unshocked ejecta in Tycho are heavily clumped it can be possible to see absorption in the LOFAR HBA even for modest amounts of unshocked mass.

5. CONCLUSIONS

In this work we have mapped Tycho's SNR with the LOFAR Low-Band and High-Band Antennae, centred at 58 MHz and 143 MHz, respectively. These are the lowest-frequency resolved observations of this source to date, even though the angular resolution of our LBA maps is modest ($41''$). We compared these maps to higher frequency VLA observations at 330 MHz and 1400 MHz (Katz-Stone et al. 2000; Williams et al. 2016), and found that in some regions the LOFAR flux is lower than expected for an unabsorbed synchrotron source. We identify this effect as low-frequency free-free absorption due to foreground free electrons absorbing the background synchrotron radiation from Tycho.

It is unlikely, from the observed geometry, that the low-frequency absorption is due to line-of-sight material far away from Tycho, but rather it must be in the environment of the SNR. There are two regions that could be responsible for the ionisation: the diffuse, infrared-emitting region immediately surrounding Tycho, or its neighbouring molecular clouds. If the former is true, and the absorption is due to an ionised cavity surrounding Tycho, then this cavity must be very thin (< 0.02 pc), so as to not contradict earlier results on the neutral fraction ahead of the shock. Alternatively, if the molecular clouds are responsible for the absorption, then the implied ionisation fraction requires an external ionising source. Tycho itself is the only candidate, through its X-ray emission, its cosmic rays, or possibly from the ionising flux of its progenitor white dwarf or the supernova explosion.

Finally, we tried to measure the free-free absorption in the region internal to the SNR reverse shock from its unshocked ejecta. However, we are limited by our knowledge of the unabsorbed spectral behaviour of the source at these frequencies: the amount of absorption we measure depends on what is the spectral index in the region, which is poorly constrained due to systematics error and an incomplete knowledge of the spectral behaviour at high frequencies. According to our best-fit scenario, the spectral index in the region internal to the reverse shock is relatively high and a copious amount of free-free absorption is required to explain the LOFAR flux densities. If real, we attribute the absorption to cold, ionised, unshocked stellar ejecta inside the SNR reverse shock free-free absorbing the synchrotron emission from the back side of the shell. In order to account for the high value of internal absorption we measure we expect the ejecta to be colder than 100 K, be somewhat highly ionised, and be heavily clumped.

Radio observations in the few GHz range could determine the unabsorbed, resolved spectral index of the source, and observations in the $200 - 1000$ MHz range would allow us to better model the parameters responsible for the absorption, which result in a characteristic

spectrum with curvature at these frequencies. Finally, hyperfine structure infrared line observations of these clumps would be necessary to better understand their temperature and composition, both critical in determining the mass in unshocked ejecta.

ACKNOWLEDGMENTS

We thank N. Kassim for the 330 MHz VLA image, and B. Williams for the 1.4 MHz VLA image.

This paper is based (in part) on data obtained with the International LOFAR Telescope (ILT) under project code LC10_011. LOFAR (van Haarlem et al. 2013) is the Low Frequency Array designed and constructed by ASTRON. It has observing, data processing, and data storage facilities in several countries, that are owned by various parties (each with their own funding sources), and that are collectively operated by the ILT foundation under a joint scientific policy. The ILT resources have benefitted from the following recent major funding sources: CNRS-INSU, Observatoire de Paris and Université d'Orléans, France; BMBF, MIWF-NRW, MPG, Germany; Science Foundation Ireland (SFI), Department of Business, Enterprise and Innovation (DBEI), Ireland; NWO, The Netherlands; The Science and Technology Facilities Council, UK.

We acknowledge the use of archival data from the National Radio Astronomy Observatory's Karl G. Jansky Very Large Array (VLA). The National Radio Astronomy Observatory is a facility of the National Science Foundation operated under cooperative agreement by Associated Universities, Inc.

Software: LOFAR Low-Frequency Pipeline (de Gasperin et al. 2019), wsclean (Offringa et al. 2014), Pre-Facet Calibration Pipeline (van Weeren et al. 2016), ddf-pipeline (v2.2; Shimwell et al. 2019), LMFIT: Non-Linear Least-Square Minimization and Curve-Fitting for Python (Newville et al. 2014), APLpy: Astronomical Plotting Library in Python (Robitaille & Bressert 2012).

Facilities: The LOw Frequency ARray (LOFAR), the Karl G. Jansky Very Large Array (VLA).

REFERENCES

Arias, M., Vink, J., de Gasperin, F., et al. 2018, A&A, 612, A110, doi: 10.1051/0004-6361/201732411

Artyukh, V. S., Dagkesamanskii, V. V., Vitkevich, R. D., & Kozhukhov, V. N. 1969, Soviet Ast., 12, 567

Baade, W. 1943, ApJ, 97, 119

Badenes, C., Borkowski, K. J., Hughes, J. P., Hwang, U., & Bravo, E. 2006, ApJ, 645, 1373, doi: 10.1086/504399

Bennett, A. S. 1963, MNRAS, 127, 3, doi: 10.1093/mnras/127.1.3

Briggs, D. S. 1995, in American Astronomical Society Meeting Abstracts, Vol. 187, 112.02

Caselli, P., Walmsley, C. M., Terzieva, R., & Herbst, E. 1998, ApJ, 499, 234, doi: 10.1086/305624

Chevalier, R. A. 1982, ApJ, 258, 790. http://adsabs.harvard.edu/cgi-bin/nph-bib_query?bibcode=1982ApJ...258..790C&db_key=AST

Conway, R. G., Daintree, E. J., & Long, R. J. 1965, MNRAS, 131, 159, doi: 10.1093/mnras/131.1.159

de Gasperin, F., Dijkema, T. J., Drabent, A., et al. 2019, A&A, 622, A5, doi: 10.1051/0004-6361/201833867

Decourchelle, A. 2017, "Supernova of 1572, Tycho's Supernova", in Handbook of Supernovae, 117, ISBN 978-3-319-21845-8. Springer International Publishing AG, doi: 10.1007/978-3-319-21846-5_48

Draine, B. T. 2011, Physics of the Interstellar and Intergalactic Medium

Duin, R. M., & Strom, R. G. 1975, A&A, 39, 33

Fanti, C., Felli, M., Ficarra, A., et al. 1974, A&AS, 16, 43

Gao, X. Y., Han, J. L., Reich, W., et al. 2011, A&A, 529, A159, doi: 10.1051/0004-6361/201016311

Ghavamian, P., Raymond, J., Hartigan, P., & Blair, W. P. 2000, ApJ, 535, 266, doi: 10.1086/308811

Gomez, H. L., Clark, C. J. R., Nozawa, T., et al. 2012, MNRAS, 420, 3557, doi: 10.1111/j.1365-2966.2011.20272.x

Green, A. J., Baker, J. R., & Landecker, T. L. 1975, A&A, 44, 187

Green, D. A. 2017, VizieR Online Data Catalog, 7278

Hayato, A., Yamaguchi, H., Tamagawa, T., et al. 2010, ApJ, 725, 894, doi: 10.1088/0004-637X/725/1/894

Hillas, A. M. 2005, Journal of Physics G Nuclear Physics, 31, R95, doi: 10.1088/0954-3899/31/5/R02

Horton, P. W., Conway, R. G., & Daintree, E. J. 1969, MNRAS, 143, 245, doi: 10.1093/mnras/143.3.245

Hurley-Walker, N., Scaife, A. M. M., Green, D. A., et al. 2009, MNRAS, 396, 365, doi: 10.1111/j.1365-2966.2009.14583.x

Hwang, U., Decourchelle, A., Holt, S. S., & Petre, R. 2002, ApJ, 581, 1101. http://adsabs.harvard.edu/cgi-bin/nph-bib_query?bibcode=2002ApJ...581.1101H&db_key=AST

Hwang, U., Hughes, J. P., & Petre, R. 1998, ApJ, 497, 833, doi: 10.1086/305501

Kassim, N. E. 1989, ApJ, 347, 915, doi: 10.1086/168183

Katz-Stone, D. M., Kassim, N. E., Lazio, T. J. W., & O'Donnell, R. 2000, ApJ, 529, 453, doi: 10.1086/308251

Kellermann, K. I., Pauliny-Toth, I. I. K., & Williams, P. J. S. 1969, ApJ, 157, 1, doi: 10.1086/150046

Klein, U., Emerson, D. T., Haslam, C. G. T., & Salter, C. J. 1979, A&A, 76, 120

Kothes, R., Fedotov, K., Foster, T. J., & Uyanıker, B. 2006, A&A, 457, 1081, doi: 10.1051/0004-6361:20065062

Krause, O., Tanaka, M., Usuda, T., et al. 2008, Nature, 456, 617, doi: 10.1038/nature07608

Langston, G., Minter, A., D'Addario, L., et al. 2000, AJ, 119, 2801, doi: 10.1086/301382

Lee, R. E., Chapman, S. C., & Dendy, R. O. 2004, ApJ, 604, 187, doi: 10.1086/381881

Lopez, L. A., Grefenstette, B. W., Reynolds, S. P., et al. 2015, ApJ, 814, 132, doi: 10.1088/0004-637X/814/2/132

McKee, C. F. 1974, ApJ, 188, 335, doi: 10.1086/152721

Milisavljevic, D., & Fesen, R. A. 2015, Science, 347, 526, doi: 10.1126/science.1261949

Newville, M., Stensitzki, T., Allen, D. B., & Ingargiola, A. 2014, LMFIT: Non-Linear Least-Square Minimization and Curve-Fitting for Python, 0.8.0, Zenodo, doi: 10.5281/ZENODO.11813

Offringa, A. R., McKinley, B., Hurley-Walker, N., et al. 2014, MNRAS, 444, 606, doi: 10.1093/mnras/stu1368

Planck Collaboration, Arnaud, M., Ashdown, M., et al. 2016, A&A, 586, A134, doi: 10.1051/0004-6361/201425022

Raymond, J. C., Koo, B. C., Lee, Y. H., et al. 2018, ApJ, 866, 128, doi: 10.3847/1538-4357/aadf93

Rest, A., Welch, D. L., Suntzeff, N. B., et al. 2008, ApJ, 681, L81, doi: 10.1086/590427

Reynolds, S. P., Borkowski, K. J., Hwang, U., et al. 2007, ApJL, 668, L135, doi: 10.1086/522830

Reynolds, S. P., & Ellison, D. C. 1992, ApJ, 399, L75, doi: 10.1086/186610

Reynoso, E. M., Moffett, D. A., Goss, W. M., et al. 1997, ApJ, 491, 816, doi: 10.1086/304997

Reynoso, E. M., Velázquez, P. F., Dubner, G. M., & Goss, W. M. 1999, AJ, 117, 1827, doi: 10.1086/300814

Robitaille, T., & Bressert, E. 2012, APLpy: Astronomical Plotting Library in Python. http://ascl.net/1208.017

Roger, R. S., Costain, C. H., & Bridle, A. H. 1973, AJ, 78, 1030, doi: 10.1086/111506

Rybicki, G. B., & Lightman, A. P. 1979, Radiative Processes in Astrophysics

Sato, T., Hughes, J. P., Williams, B. J., & Morii, M. 2019, arXiv e-prints, arXiv:1903.00764. https://arxiv.org/abs/1903.00764

Scott, P. F., & Shakeshaft, J. R. 1971, MNRAS, 154, 19P, doi: 10.1093/mnras/154.1.19P

Shimwell, T. W., Röttgering, H. J. A., Best, P. N., et al. 2017, A&A, 598, A104, doi: 10.1051/0004-6361/201629313

Shimwell, T. W., Tasse, C., Hardcastle, M. J., et al. 2019, A&A, 622, A1, doi: 10.1051/0004-6361/201833559

Smirnov, O. M., & Tasse, C. 2015, MNRAS, 449, 2668, doi: 10.1093/mnras/stv418

Snow, T. P., & McCall, B. J. 2006, ARA&A, 44, 367, doi: 10.1146/annurev.astro.43.072103.150624

Tasse, C. 2014a, arXiv e-prints. https://arxiv.org/abs/1410.8706

—. 2014b, A&A, 566, A127, doi: 10.1051/0004-6361/201423503

—. in preparation

Tasse, C., Hugo, B., Mirmont, M., et al. 2018, A&A, 611, A87, doi: 10.1051/0004-6361/201731474

Tian, W. W., & Leahy, D. A. 2011, ApJ, 729, L15, doi: 10.1088/2041-8205/729/2/L15

van Haarlem, M. P., Wise, M. W., Gunst, A. W., et al. 2013, A&A, 556, A2, doi: 10.1051/0004-6361/201220873

van Weeren, R. J., Williams, W. L., Hardcastle, M. J., et al. 2016, ApJS, 223, 2, doi: 10.3847/0067-0049/223/1/2

Vinyaikin, E. N., Volodin, Y. V., Dagkesamanskii, R. D., & Sokolov, K. P. 1987, Soviet Ast., 31, 141

Warren, J. S., et al. 2005, ApJ, 634, 376, doi: 10.1086/496941

Williams, B. J., Borkowski, K. J., Ghavamian, P., et al. 2013, ApJ, 770, 129, doi: 10.1088/0004-637X/770/2/129

Williams, P. J. S., Kenderdine, S., & Baldwin, J. E. 1966, MmRAS, 70, 53

Williams, W. L., van Weeren, R. J., Röttgering, H. J. A., et al. 2016, MNRAS, 460, 2385, doi: 10.1093/mnras/stw1056

Woods, T. E., Ghavamian, P., Badenes, C., & Gilfanov, M. 2017, Nature Astronomy, 1, 800, doi: 10.1038/s41550-017-0263-5

Zhou, P., Chen, Y., Zhang, Z.-Y., et al. 2016, ApJ, 826, 34, doi: 10.3847/0004-637X/826/1/34